
Theses and Dissertations

Summer 2012

Pixel classification of iris transillumination defects

Umme Salma Yusuf Bengali
University of Iowa

Follow this and additional works at: <https://ir.uiowa.edu/etd>



Part of the [Biomedical Engineering and Bioengineering Commons](#)

Copyright 2012 Umme Salma Yusuf Bengali

This thesis is available at Iowa Research Online: <https://ir.uiowa.edu/etd/3260>

Recommended Citation

Bengali, Umme Salma Yusuf. "Pixel classification of iris transillumination defects." MS (Master of Science) thesis, University of Iowa, 2012.
<https://doi.org/10.17077/etd.2pyr86tc>

Follow this and additional works at: <https://ir.uiowa.edu/etd>



Part of the [Biomedical Engineering and Bioengineering Commons](#)

PIXEL CLASSIFICATION OF IRIS TRANSILLUMINATION DEFECTS

by

Umme Salma Yusuf Bengali

A thesis submitted in partial fulfillment
of the requirements for the Master of
Science degree in Biomedical Engineering
in the Graduate College of
The University of Iowa

July 2012

Thesis Supervisor: Professor Joseph M. Reinhardt

Graduate College
The University of Iowa
Iowa City, Iowa

CERTIFICATE OF APPROVAL

MASTER'S THESIS

This is to certify that the Master's thesis of

Umme Salma Yusuf Bengali

has been approved by the Examining Committee
for the thesis requirement for the Master of Science
degree in Biomedical Engineering at the July 2012 graduation.

Thesis Committee:

Joseph M. Reinhardt, Thesis Supervisor

Michael D. Abramoff

Wallace L.M. Alward

ACKNOWLEDGEMENTS

I would like to express my gratitude to Dr. Wallace L.M. Alward for giving me the opportunity to work on this project. It has been a very valuable and interesting experience for me during which I have learned many important image processing concepts.

I am sincerely thankful to Dr. Joseph M. Reinhardt for providing me with a lot of assistance in the early stages of the project that helped everything fall into place, and for always being available to answer my questions. I am very grateful for Dr. Michael D. Abramoff's enthusiastic assistance and encouragement which has been instrumental in enabling me to understand the different concepts that were required to implement this project.

I am grateful for the guidance provided by my lab mates Xiayu, Vinayak and Richard, and I am very appreciative of Sandeep's assistance in important stages of the project.

I would also like to thank members of the Ophthalmology research group – Dr. Mona K. Garvin, Dr. Todd E. Scheetz, Dr. Li Tang, Mark Christopher, and Qiao Hu for providing valuable insights and ideas for solving the problems that I faced during this project.

My family's support has been crucial in helping me succeed in my Master's studies, for which I am always thankful.

I would especially like to thank my friend Mansa for her encouragement and motivation over the past two years, and Mrinay for his ever cheerful support. I am also thankful for the support from all of my friends which has been invaluable while adjusting to life in a new country.

Lastly, I would like to thank all the people I have come to know who made my time at the University of Iowa a memorable one.

TABLE OF CONTENTS

LIST OF TABLES	iv
LIST OF FIGURES	v
CHAPTER	
1. INTRODUCTION	1
2. BACKGROUND AND SIGNIFICANCE	3
2.1 Eye Anatomy Overview	3
2.2 Mechanism of Pigment Dispersion	4
2.3 Pigment Dispersion Syndrome	5
2.4 Automated and Computer Assisted Detection of Eye Diseases	5
2.5 K-Nearest Neighbors Classification Overview	6
2.6 Previous work	7
3. METHODOLOGY	8
3.1 Overview	8
3.2 Image Acquisition	10
3.3 Image Segmentation	12
3.4 Reference Standard Images	12
3.5 Feature Calculation	13
3.6 Feature Selection	18
3.7 Training Sample Selection	20
3.8 KNN Classification	21
3.9 Implementation	23
4. RESULTS	24
4.1 Image Segmentation Results	24
4.2 Feature Calculation Results	25
4.3 Feature Selection Results	28
4.4 KNN Classification Results	28
5. DISCUSSION	33
6. CONCLUSION	34
APPENDIX	35
REFERENCES	39

LIST OF TABLES

Table

- A1. The data of each subject included in this research with their diagnoses as follows - *PG*: Pigment Dispersion Syndrome with elevated pressures and glaucomatous nerves, *PDS*: Pigment Dispersion Syndrome with normal pressure and nerves, *PDS w/ OHT*: Pigment Dispersion Syndrome with elevated pressures but normal nerves35
- A2. A list of the parameter values for each subject's eye image showing the inputs to the Hough transform in order to segment out the iris regions, with each value representing the number of pixels37

LIST OF FIGURES

Figure

2.1. Diagram of eye anatomy	3
3.1. Block diagram of methodology	9
3.2. Examination of a patient's eyes using a combination of infrared and visible light	10
3.3. An eye affected by pigment dispersion syndrome. The iris areas where pigment has been lost have a brighter intensity than the surrounding regions	11
3.4. A Gaussian kernel with mean = 0 and standard deviation = $\sqrt{2}$	13
3.5. A difference of Gaussians kernel with $\sigma_1 = 2$ and $\sigma_2 = 4$ used for edge detection	15
3.6. A Gaussian derivative kernel with $\sigma = 2$ used for edge detection	16
3.7. An example Laplacian of Gaussian kernel used for edge detection	17
3.8. Mirroring of iris region boundaries: (a) A segmented iris image converted to the Cartesian domain. (b) The standard deviation calculated using a 3x3 neighborhood showing a bright upper and lower boundary. (c) Segmented iris image with mirrored boundaries. (d) Corresponding feature image with standard deviation calculated using a 3x3 neighborhood	17
3.9. Linear forward selection: (a) The fixed set technique. (b) The fixed width technique	19
3.10. An example of KNN classification in a 2-dimensional feature space with features $f1$ and $f2$ with $k=5$. Circles and squares represent members of the two classes. A prediction is calculated for the element under consideration	21
4.1. Image segmentation result example: (a) The original eye image for subject number 14. (b) The iris extracted by the Hough transform with pupil radius 72 pixels and outer iris radius 255 pixels. (c) The extracted iris region converted to Cartesian coordinates	25
4.2. Feature calculation results examples: (a) Standard deviation with a neighborhood of 3x3. (b) Standard deviation with a neighborhood of 5x5. (c) Standard deviation with a neighborhood of 3x9. (d) Difference of Gaussians with $\sigma_1 = 1$ and $\sigma_2 = 2$. (e) Difference of Gaussians with $\sigma_1 = 2$ and $\sigma_2 = 4$. (f) Gradient Magnitude image. (g) Average intensity image. (h) Gaussian derivative of image along the X-axis. (i) Gaussian derivative of image along the Y-axis. (j) Laplacian of image	26

4.3. KNN classification results example: (a) The segmented iris region in the Cartesian domain for subject number 14. (b) The probability image with 21 gray levels showing the likelihood of each pixel belonging to a defect region. (c) The probability image converted back to the polar domain. (d) The truth image with defect regions manually outlined	28
4.4. Some results of the kNN classification: (a) This column of images is the iris regions that were manually segmented out for subject numbers 9, 16, 40 and 43. (b) The truth images showing the defect regions manually outlined. (c) The probability images with a threshold of 3/21 applied showing predicted output of the KNN classifier	29
4.5. The ROC curve for the KNN classification output.....	31

CHAPTER 1

INTRODUCTION

Glaucoma is a group of diseases of the optic nerve of the eye. One of the main causes is increased pressure in the eye, related to insufficient drainage of intraocular aqueous fluid through the trabecular meshwork. Glaucoma results in damage to the optic nerve leading to visual field loss, and blindness if left untreated [1]. It is a disease that can affect any person, but high-risk categories do exist. In the United States, it is estimated that 2 million people have glaucoma, and this number is projected to increase by 2020 to more than 3 million [9].

Open-angle glaucoma (OAG) is a type of glaucoma where the aqueous humor from the eye does not drain normally and builds up. This fluid buildup exerts pressure on the optic nerve and over time causes loss of nerve fibers and eventually loss of vision. OAG is hard to detect because patients do not notice the early symptoms such as blank spots in the visual field and it becomes symptomatic only when the damage is extensive. Glaucoma damage is irreversible.

One variant of OAG is pigmentary glaucoma. Pigmentary glaucoma is defined as a secondary open-angle glaucoma because it is the result of another medical condition: pigment dispersion syndrome. Pigment dispersion syndrome (PDS) occurs when unusual amounts of pigment are lost from the posterior surface of a patient's iris. The pigment then gets deposited in the anterior and posterior chambers of the eye including the trabecular meshwork, where it reduces aqueous outflow [2]. An estimated 25% to 50% of patients with PDS develop pigmentary glaucoma [2] and PDS is one of the markers of the risk of developing pigmentary glaucoma.

Approximately 0.9% to 2.5% of glaucoma cases in the United States are diagnosed as pigmentary glaucoma [6]. This constitutes a significant number of people

affected by this type of glaucoma. Importantly, while most forms of glaucoma affect the elderly, pigmentary glaucoma usually affects those in the third or fourth decades of life.

This thesis examines a pixel classification technique to identify regions of pigment lost from the iris and distinguish them from unaffected iris tissue which has normal pigment variation. Several steps are involved in this process as follows:

1. Segmentation of the iris region using the Hough transform,
2. Feature calculation for pixel classification,
3. Feature selection,
4. Pixel classification using the K-nearest neighbors (kNN) classification algorithm.

The final probability image generated using the output of the kNN algorithm will show the likelihood of pixels belonging either to defect or normal regions. The following chapter explains in detail how pigment dispersion syndrome develops, and the motivation behind using the kNN algorithm for pixel classification.

CHAPTER 2

BACKGROUND AND SIGNIFICANCE

2.1 Eye Anatomy Overview

In order to understand the mechanism of pigment dispersion syndrome and pigmentary glaucoma, it is necessary to introduce the structure of the eye.

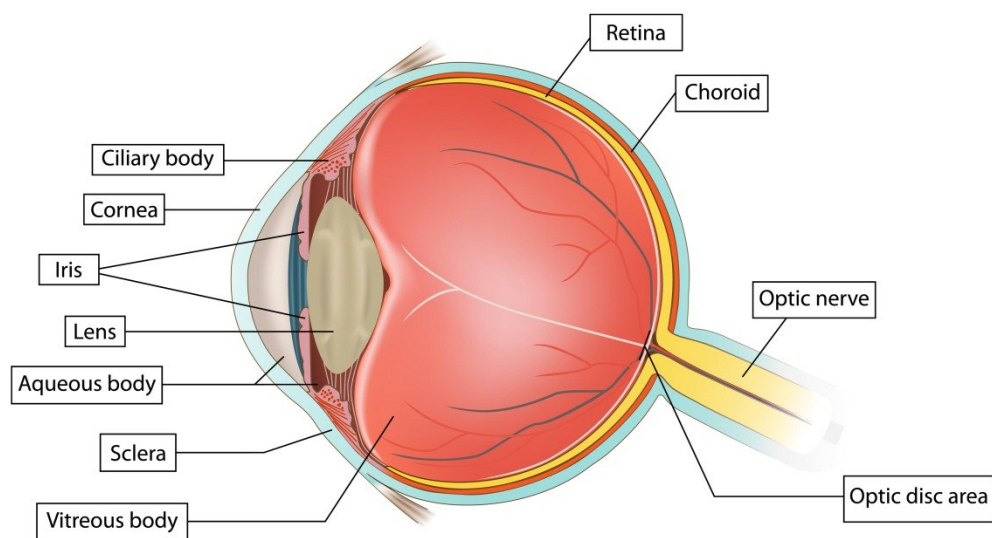


Figure 2.1: Diagram of eye anatomy (Figure from [15]).

The eye has three layers and is filled with fluid that is present in two chambers. The white capsule around the eye is called the sclera, which is specialized at the anterior surface of the eye as the cornea. The cornea is composed of clear tissue. The darkly pigmented choroid layer absorbs light rays at the back of the eye. In the front of the eye,

it is specialized to form the iris, the ciliary muscles and zonular fibers. The pupil is an anterior opening in the iris that lets light enter the eye. The iris has circular and radial smooth muscles that control the pupil diameter. The crystalline lens is located just behind the iris whose shape is controlled by the ciliary muscle and zonular fibers. The retina lines the inner, posterior surface of the eye and it is an extension of the brain. The fovea centralis is a region that is specialized to deliver the highest visual acuity. The optic disc is where the nerve fibers that carry information from ganglion cells and photoreceptors located on the retina exit the eye as the optic nerve. The anterior chamber of the eye located between the iris and the cornea contains a clear fluid called aqueous humor. Aqueous humor flows in and out of the anterior chamber, and it flows out at the open angle where the iris and cornea meet, in the region called the trabecular meshwork [1]. The posterior chamber of the eye located between the lens and the retina is filled with vitreous, a viscous, jellylike substance [7].

2.2 Pigment Dispersion Mechanism

When pigment is lost from the posterior surface of the iris, it is deposited in the anterior and posterior chambers of the eye. One theory of the mechanism of pigment loss states that backbowing of the iris causes the pigment epithelium to come in contact with packets of lens zonules [8]. The friction caused by this contact disrupts epithelial cells and causes melanosomes to be released into the aqueous humor. The melanosomes collect in the trabecular meshwork causing a rise in intraocular pressure (IOP). The endothelial cells of the trabecular meshwork act to phagocytize the melanosomes, and if regular pigment release from the iris occurs, then it leads to a chronic rise in IOP [2]. This IOP rise can lead to pigmentary glaucoma.

2.3 Pigment Dispersion Syndrome

Pigment dispersion syndrome (PDS) may be diagnosed in patients in the second decade of life, but is usually diagnosed by 30 years of age and later. It occurs equally in men and women, but men are more likely to develop pigmentary glaucoma [2]. Other genetic factors that predispose people to developing PDS are Caucasian race, myopia, and the presence of family members diagnosed with PDS [16].

PDS usually produces no symptoms, although occasionally patients may experience blurred vision and halos with high impact activities which are caused by a rise in IOP.

The physical signs of PDS can be seen in several structures of the eye: the cornea, iris, pupil, and the angle between the iris and cornea. This thesis deals with the effects of PDS on the iris, called transillumination defects. They are called so because the loss of pigment from the iris can be visualized through transillumination, which is the illumination of body tissue by transmitting light through it. Initially, transillumination defects are usually slit-like, and as pigment loss increases, the defects become irregularly shaped.

2.4 Automated and Computer Assisted Detection of Eye Diseases

Automated and computer assisted detection of eye diseases is meant to assist physicians in detecting, managing and treating eye diseases. One form of automated and computer assisted detection is Computer Aided Diagnosis or CAD.

Xu et al. [19] and Abramoff et al. [21] used pixel feature classification to detect structures in the eye like the optic disc which can prove useful for discovering the extent of primary glaucoma. Bock et al. [22] used a Support Vector Machine (SVM) classifier to automatically quantify the probability that a patient will suffer from glaucoma by analyzing color fundus images.

CAD has been used outside the eye to detect lung diseases like Chronic Obstructive Pulmonary Disease (COPD) [25] by identifying features on CT scans that are indicative of the presence of disease. CAD has also been used for the purpose of detecting breast cancer lesions from CT scans [26] and in the segmentation of heart vessels [27].

This thesis uses pixel feature classification to automatically detect regions of pigment dispersion in a patient's iris.

2.5 K-Nearest Neighbors Classification Overview

Classification algorithms, such as the K-nearest neighbors (kNN) classification algorithm used in this thesis, are used to predict the class of an element under consideration, given a set of training examples. KNN is a nonparametric classification technique which requires no prior knowledge of the distribution of data to be classified and does not require elaborate training. Two stages are involved in the classification: a training stage and a deployment or testing stage. In the training stage, vectors of features along with their associated class labels are given as inputs to the classifier. When the classifier is given a test vector to classify, it traverses the training vectors and calculates the distance, for example Euclidean distance, to each training vector. After calculating the distance metric, the k nearest in distance neighbors are found for the vector to be classified. This is done by assigning to the element the class label of the majority of neighbors. The class label that is assigned is the label for that test vector. Examples of the use of kNN in disease diagnosis are for glaucoma detection [21] and the detection of retinal vessels [28].

2.6 Previous Work

The amount of pigment lost from the surface of the iris is associated to the risk of developing or worsening pigmentary glaucoma. Thus, it is of interest to keep track of the

changes in the degree of pigment loss. Up until now, no method has been proposed for automated detection of pigment dispersion. Haynes et al. [3] used manual tracing of the regions of pigment loss in the iris to measure the amount of pigment lost from it. Roberts et al. [10] also employed manual tracing while examining the best technique for imaging the iris defects.

Manual tracing of defect regions was first performed by Haynes et al. [3] by outlining desired regions using a pen and digitizer tablet. The entire iris region area was found by subtracting the area of the pupil from the area of the pupil plus the iris. Each transillumination defect area was also outlined. The percent transillumination was found by dividing the total area of defect regions by the total area of the iris. This process was carried out for each iris image from 13 patients. For a larger dataset of patients this would be quite tedious and time consuming, as well as being prone to errors if the measurements were taken by different observers for the same patient. This was observed by Haynes et al. [3] when the inter-observer coefficient of variation for three standard images was found to be quite high at 20.35, 6.55 and 8.01% respectively for mild, moderate, and marked transillumination. The intra-observer coefficient of variation was found to be lower at 4.11, 3.23 and 2.38% respectively for mild, moderate, and marked transillumination. However, it cannot always be expected that the same observer will be available to take manual measurements of the percent transillumination.

Roberts et al. [10] also performed manual tracing of the transillumination defect regions using computer graphics software. However their aim was to find the best wavelength of light to visualize the transillumination defects and not to quantify the amount of transillumination. Their results agreed with the conclusion of Alward et al. [4] who also found that defect regions are best observed using a combination of infrared and visible light.

CHAPTER 3

METHODOLOGY

3.1 Overview

Several pre-processing steps of an iris image are required before classification can be carried out. First, image segmentation is required to extract the iris region from the images so that classification is not thrown off by spurious pixels that appear as belonging to the iris.

After the segmentation stage, converting the images to the polar domain is performed to make the random selection of pixels for training the classifier less complex because of the resulting rectangular image shape. A diverse set of features was then calculated from the image in the polar domain.

Given a set of images for which the features had thus been calculated, feature selection was performed to optimize the size of the feature set and remove any redundant features.

To evaluate the performance, a reference standard is needed. An expert manually marked the transillumination pixels on each test image, and these markings were then verified by a glaucoma expert. Given this reference standard, training and evaluation of the kNN classifier was carried out. The result of kNN classification is a probability image with k gray levels showing the probability of each pixel belonging to a defect region. This probability image was then converted back to the Cartesian domain. The entire process is shown in Figure 3.1.

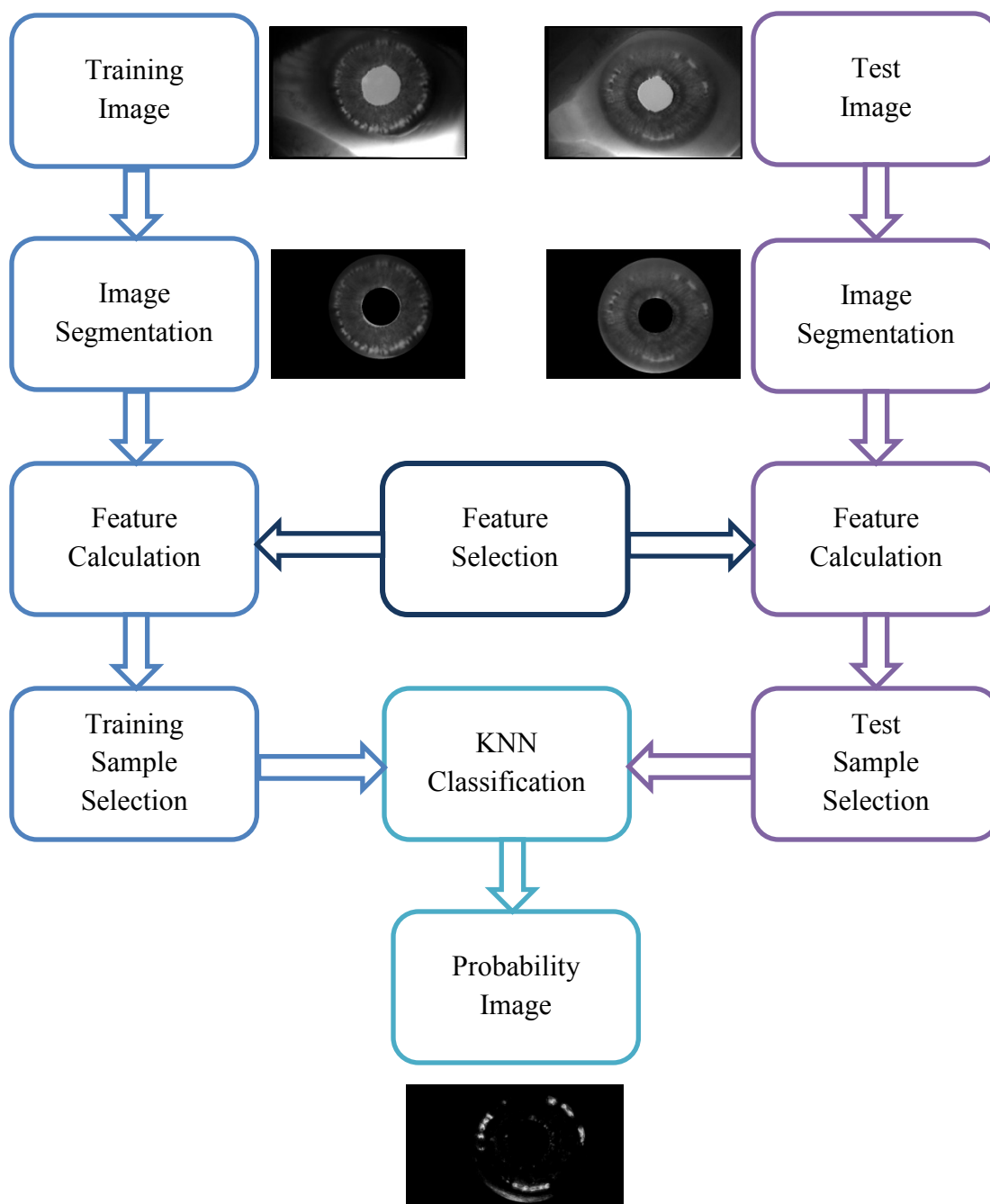


Figure 3.1: Block diagram of methodology

3.2 Image Acquisition

Since the cause of PDS and subsequently pigmentary glaucoma is the loss of pigment from the posterior surface of the iris, the conditions are characterized by radially oriented, slit-like transillumination defects in the mid-peripheral iris. In this study, the images were obtained through infrared transillumination by Alward et al. [4]. Infrared transillumination of the iris is used by ophthalmologists to detect iris pigment defects that could indicate disease [29 – 31].

Patients with pigmentary glaucoma or pigment dispersion syndrome were selected from the Glaucoma Service at the University of Iowa, Iowa City. The setup to capture the images is shown in Figure 3.2.



Figure 3.2: Examination of a patient's eyes using a combination of near infrared and visible light (Figure from [4]).

Each patient's head was positioned in a headrest mounted in front of a black and white video camera sensitive to light in the near infrared range. The camera (RCA TC77011/U RCA Inc., Lancaster, PA) was equipped with a macro/zoom lens (Javelin 99035 J, 18-108 mm, f2.5, Javelin Electronics Inc., Torrance, CA). A halogen fiber optic transilluminator was used as a cool light source producing a mixture of visible and infrared light [4]. Either the visible or infrared light could be filtered out at the source or at the camera.

As a result of using visible light, the pupil dilation of patients' eyes was minimized and resulted in an enhanced picture of the transillumination defects. The use of near infrared light helped to clearly visualize transillumination defects. Videos of patients' eyes were recorded by a 0.75-inch videocassette machine (Sony V05600 "u-matic," Sony Corp of America, Teaneck, NJ) [4]. The videos were digitized and frames were extracted to be used for analysis.

An example case of pigment dispersion syndrome is shown in Figure 3.3:

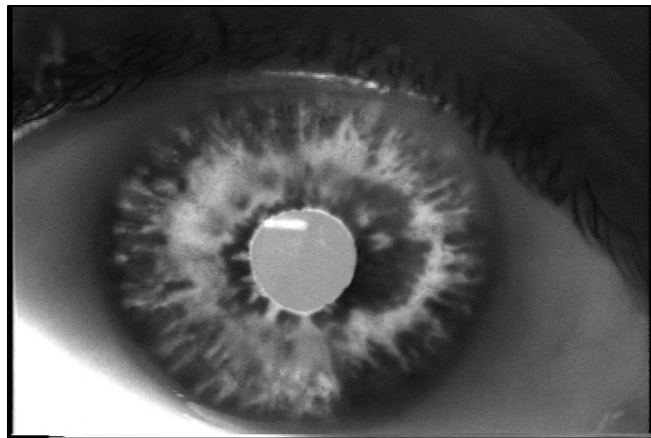


Figure 3.3: An eye affected by pigment dispersion syndrome. The iris areas where pigment has been lost have a brighter intensity than the surrounding regions.

A list of the iris images of subjects used in this study along with their corresponding data is given in the appendix Table A.1. The data of 38 out of 50 subjects showed that they were diagnosed with either pigment dispersion syndrome or pigmentary glaucoma. Information about the remaining subjects could not be retrieved.

3.3 Image Segmentation

The raw images of the patients' eyes which were obtained using a combination of infrared and visible light contain other features of the eye, which are not of interest in determining the amount of iris transillumination. If these features are not removed, it would result in the kNN classifier giving false positive results. The Hough transform was used to detect the pupil and iris boundaries, and extract the iris regions from the images.

The segmented images now contained only iris tissue and were suitable for further processing steps. To train the kNN classifier, a random number of pixels had to be selected from the segmented images and it was determined that the process of random selection would be less complex if the images were converted to the polar coordinate system. The circular iris region was thus transformed into a rectangular region.

3.4 Reference Standard Images

The kNN classifier training stage requires a reference standard image for each pixel in order to know which combinations of features amount to an iris transillumination defect (ITD) region and which ones do not. Reference standard images were generated using the 'Truthmarker' app [14] created in our group on an iPad and they were verified by Dr. Wallace L.M. Alward. Fifty segmented images were used and the defect regions were outlined. The annotated images were then converted to binary with the defect regions colored white and all other regions colored black. As was done with the original iris images, the reference standard images were also converted to polar coordinates.

3.5 Feature Calculation

Classification of defect and normal iris regions requires a set of features to be calculated and given as input to the kNN classifier.

A detailed description of the features is as follows:

1. *Standard Deviation*: The standard deviation of a pixel with a specified neighborhood provides a texture descriptor [33].

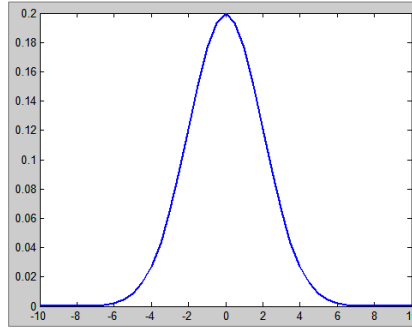


Figure 3.4: A Gaussian kernel with mean = 0 and standard deviation = $\sqrt{2}$

Since the iris defects have a higher intensity compared to normal iris tissue, standard deviation provides a useful texture feature for classification. In order to remove noise, the image was first convolved with a Gaussian kernel. A Gaussian kernel is a bell shaped curve as shown in Figure 3.4, with a specified standard deviation: σ . It is given by the equation:

$$G_{\sigma}(x, y) = \frac{1}{2\pi\sigma^2} e^{-\frac{x^2+y^2}{2\sigma^2}}$$

The image was convolved with a Gaussian kernel with $\sigma=2$. Next, the standard deviation was calculated at three different neighborhoods: 3x3, 5x5 and a rectangular neighborhood 3x9. The standard deviation of a pixel's intensity in a specific neighborhood is given by the equation:

$$\sigma = \sqrt{\frac{\sum (I_{(x,y)} - \bar{I}_{(x,y)})^2}{n - 1}}$$

n is the number of pixels in the neighborhood, $I_{(x,y)}$ is the intensity of the pixel under consideration, and $\bar{I}_{(x,y)}$ is the mean of all the pixels in that neighborhood. A large standard deviation value indicated a large variation in intensity in that neighborhood which occurs around the ITD regions. For example consider a pixel with intensity value 123 and its 3x3 neighborhood:

161	134	133
148	123	120
137	132	109

The standard deviation of the center pixel will be equal to 16 according to the given equation.

2. *Difference of Gaussians*: This feature emphasizes edges in the image [32] by subtracting the convolution results of the image I with two Gaussian kernels G_1 and G_2 by the equation:

$$I * G_2 - I * G_1$$

Two feature images were obtained: one by using the value of standard deviation $\sigma=1$ for G_1 and $\sigma=2$ for G_2 , and the other by using $\sigma=2$ for G_1 and $\sigma=4$ for G_2 .

One of the kernels used is shown in Figure 3.5:

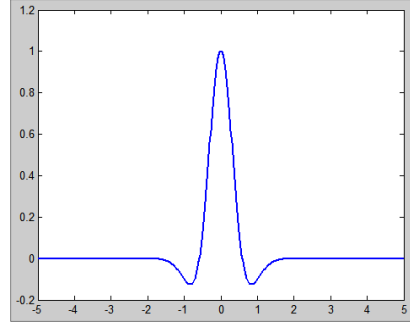


Figure 3.5: A difference of Gaussians kernel with $\sigma_1 = 2$ and $\sigma_2 = 4$ used for edge detection.

3. *Gradient Magnitude*: The gradient magnitude operator detects intensity discontinuities by calculating the magnitude of the gradient vector [32]. Thus it detects edges in an image. First, the image is convolved with a Gaussian kernel with $\sigma=2$ as shown in Figure 3.4 in order to remove noise from the image because this operator is very sensitive to noise. Next, the gradient magnitude of the image was calculated. The gradient magnitude is found by using the equation:

$$|\nabla I| = \sqrt{\left(\frac{\partial I}{\partial x}\right)^2 + \left(\frac{\partial I}{\partial y}\right)^2}$$

4. *Average Intensity*: An intensity feature is very useful for detecting iris defects [33] because the iris transillumination defect regions have a higher intensity compared to normal iris tissue. The average intensity of a pixel in a 3x3 neighborhood was found and used as a feature for classification as shown in the equation below:

$$\sum_{i=1}^n \frac{I_{(x,y)_i}}{n}$$

where n is the number of pixels in the neighborhood.

5. *Gaussian Derivative*: The Gaussian derivative is used to detect edges in the image, separating out different homogeneous regions in the iris images [33]. The Gaussian derivative kernel is as shown in Figure 3.6:

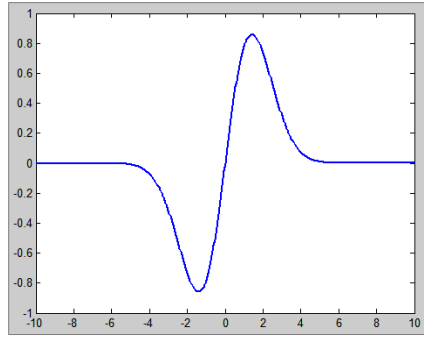


Figure 3.6: A Gaussian derivative kernel with $\sigma=2$ used for edge detection.

The Gaussian derivative in the horizontal as well as the vertical direction with $\sigma = 2$ was calculated. The equation for calculating the Gaussian derivative is:

$$\frac{\partial}{\partial \mathbf{x}} G_{\sigma}(\mathbf{x}, \mathbf{y}) = \frac{\partial}{\partial \mathbf{x}} \left(\frac{1}{2\pi\sigma^2} e^{-\frac{\mathbf{x}^2 + \mathbf{y}^2}{2\sigma^2}} \right)$$

6. *Laplacian of Gaussian*: The Laplacian of Gaussian is a derivative filter that can detect intensity changes in an image, thus emphasizing edges [34].

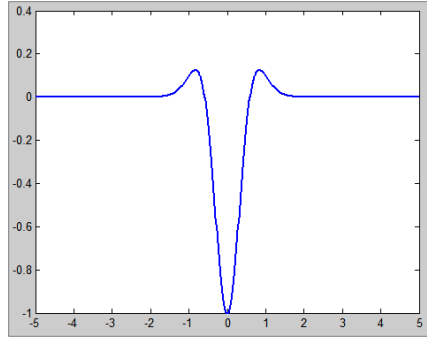


Figure 3.7: An example Laplacian of Gaussian kernel used for edge detection.

A Laplacian kernel is shown in Figure 3.7. It calculates the second derivative of the image given by the equation:

$$LoG = \frac{\partial^2}{\partial x^2} G_{\sigma}(x, y) + \frac{\partial^2}{\partial y^2} G_{\sigma}(x, y)$$

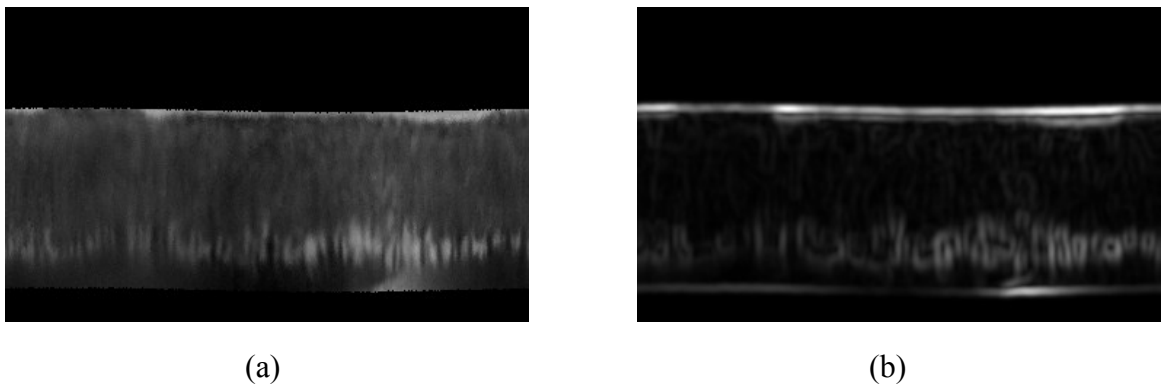
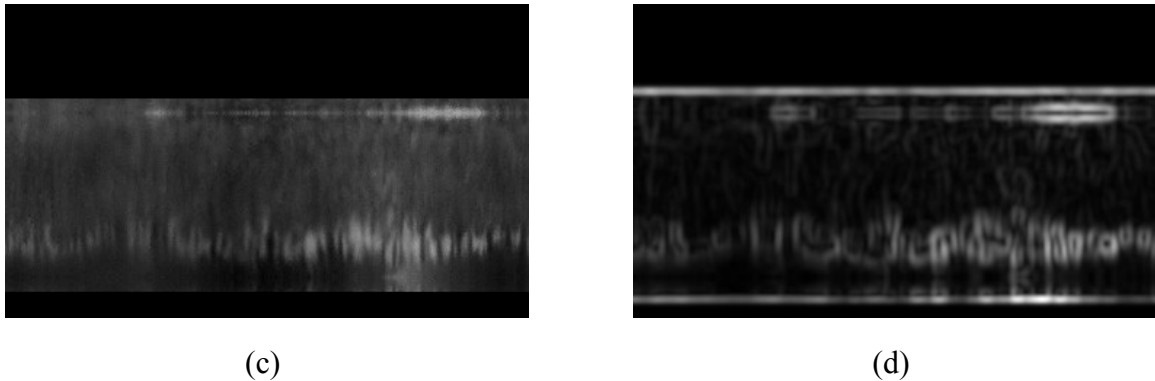


Figure 3.8: Mirroring of iris region boundaries: (a) A segmented iris image converted to the Polar domain. (b) The standard deviation calculated using a 3x3 neighborhood showing a bright upper and lower boundary. (c) Segmented iris image with mirrored boundaries. (d) Corresponding feature image with standard deviation calculated using a 3x3 neighborhood.

Figure 3.8 continued -



During the initial stages of testing the kNN classifier, it was found that the feature calculation process was producing a bright boundary between the iris region and the black background in the polar domain images as shown in Figure 3.8 (b).

These bright boundaries resulted in the kNN classifier producing false positives. In order to prevent this misclassification, the original segmented iris image boundaries were mirrored by 10 rows. After mirroring the boundaries, the features were re-calculated, as seen in Figure 3.8 (d). Following this process, feature selection performed.

3.6 Feature Selection

Ten feature images each of fifty segmented iris images were obtained following the feature calculation stage. The set of feature images of twenty segmented images was used for optimal feature selection, and the remaining set of thirty segmented images was used for training and testing the kNN classifier.

Before performing kNN classification it is useful to carry out optimal feature selection. Feature selection helps to reduce the number of irrelevant features which in turn will reduce the running time of the classification, as well as increase its accuracy

[17]. There are two types of feature selection algorithms: feature subset selection and dimensionality reduction. In this research, a type of feature subset selection algorithm was used called linear forward selection.

Linear forward selection is derived from another technique of feature selection called sequential forward selection. Sequential forward selection works by starting with the empty subset of selected features. It then evaluates all possibilities of expanding the subset by a single attribute. If an attribute leads to the best score, it is permanently added to the subset. The search for attributes ends when no attribute can be found that improves the current best score.

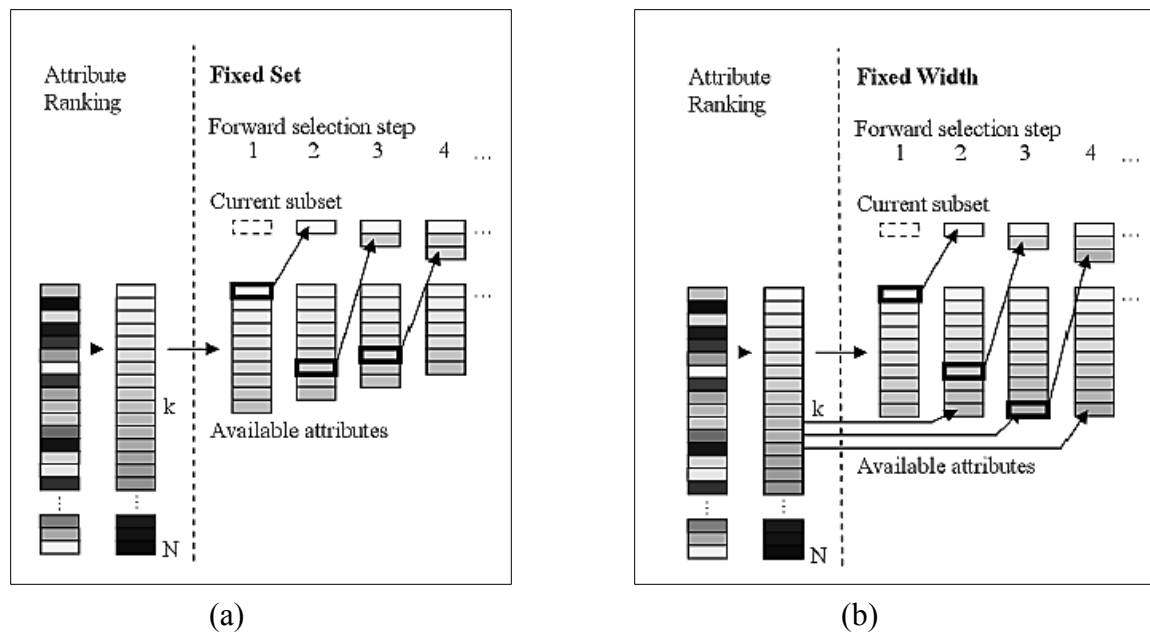


Figure 3.9: Linear forward selection: (a) The fixed set technique. (b) The fixed width technique. (Figure from [18])

Linear forward selection improves upon the run time of sequential forward selection. There are two types of linear forward selection: fixed width and fixed set technique which can limit the number of attributes.

In the fixed set technique shown in Figure 3.9 (a), all the attributes are ranked and the top k ranked attributes are selected as input to the linear forward selection. The initial ranking of attributes is done by evaluating each one individually and ranking them according to their scores.

The second column in Figure 3.9 (a) shows the ranking of attributes. The attributes that are not selected are discarded. The process of subset selection is shown on the right of Figure 3.9 (a). The number of subset extensions decreases while the currently selected subset increases in number. It is called the fixed set technique because it results in a set of selected attributes of size k .

In the fixed width technique shown in Figure 3.9 (b), the attributes are also ranked and the top k attributes are the input to the linear forward selection. As the forward selection proceeds, the attributes added to the subset are selected from the next best attribute in the ranking. As a result, it is ensured that the set of candidate expansions consists of the individually best k attributes that have not been selected so far during the search. The technique is called fixed width technique because it keeps the number of extensions in each forward selection step constant at a fixed width k .

Training data was collected from the images and given as input to WEKA [24], a collection of machine learning algorithms. The feature selection algorithm was selected as linear forward selection along with cross validation for the attribute selection mode.

3.7 Training Sample Selection

A fixed number of random pixels were selected from the training feature images to be given as input to the pixel classifier. A random selection of image pixels was taken because variability in the training data is required. Since the images that were converted

to Polar space have a black background left over from the segmentation stage, it was ensured that no training pixels were selected from the background. This would have resulted in training data of no significance.

3.8 KNN Classification

The kNN classification process is carried out by training the classifier using the feature images and testing it on a dataset that is unknown to it. An example vector for training would have values such as:

$$[13 \ 17 \ 116 \ 126 \ 72 \ 12 \ 21 \ 0]$$

with each vector element representing a feature for the pixel. The label is 0 or 1 depending on whether that combination of features corresponds to a normal or defect region respectively in the corresponding reference standard image.

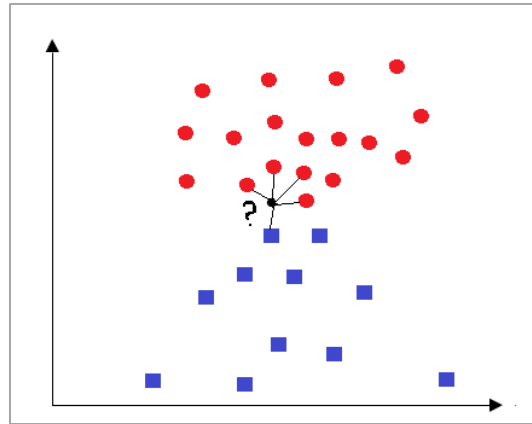


Figure 3.10: An example of kNN classification in a 2-dimensional feature space with features $f1$ and $f2$ with $k=5$. Circles and squares represent members of the two classes. A prediction is calculated for the element under consideration.

An example of kNN classification is shown in Figure 3.10. The value of k was chosen to be an odd number to avoid the possibility of ties. After experimenting with various odd values for k , the value 21 was selected because it gave better results compared to $k = 3, 9$, or 11. The two possible class labels are normal and defect pixel. In order to improve the prediction of class labels, a weight may be applied to the calculation of distance values. The neighbors of the test element vote for the predicted class with votes weighted by the reciprocal of their distance to the test element.

In this research the Approximate Nearest Neighbors (ANN) library created by Mount and Arya [14] was used for classification purposes. The distances from a pixel to its neighbors are measured using the squared distance and not the true Euclidean distance. The equation for true Euclidean distance is:

$$dist(p, q) = \left(\sum_{0 \leq i < d} (p_i - q_i)^2 \right)^{1/2}$$

Using squared distances helps to represent distances as integers when integer type elements are used as well as saves on computation time. The distance metric can be changed according to the user's preferences.

The ANN program can be given an error bound $\epsilon \geq 0$ which is used for approximate nearest neighbor searching. If this is specified, then the i^{th} nearest neighbor of a query point is a $(1 + \epsilon)$ approximation to the true i^{th} neighbor. This means that the true Euclidean distance to a point from the query point may exceed the distance to the real i^{th} nearest neighbor by a factor of $(1 + \epsilon)$. Employing an approximate k nearest neighbor search will significantly improve the running time. However, the pre-processing time depends on the number of points in the training set and the dimension of the feature space, and is independent of the error bound ϵ .

The process of leave-one-out cross validation was used for thirty patient images. Twenty nine images were used as training images, and one image was the test image.

This process was repeated thirty times, each time rotating among the dataset, so that no image was picked as the test image twice. Cross validation provides a good idea of how the classifier is performing by reducing the variance of estimation, and also needs to be used because of the small data set of images.

3.9 Implementation

The code for all the steps involved in the methodology was written using the Insight Toolkit (ITK) version 3.20.0. For the manual segmentation of images using the Hough transform, the code was adapted from Mosaliganti et al. [12] who implemented a faster version of the transform which also gives more accurate results than the built-in ITK version. The different features were calculated using built-in ITK filters as well as by modifying some of the filters to obtain desired results. Feature selection was performed using WEKA [24] as explained in Section 3.6. The kNN classification process was performed using the ANN library created by Mount and Arya [14]. This library has customizable features such as supporting both exact and approximate nearest neighbor searching and supporting the use of any Minkowski distance metric including Manhattan, Euclidean and Max metrics. The ROC curve shown in chapter 4 was plotted using the online calculator created by Eng [23].

CHAPTER 4

RESULTS

4.1 Image Segmentation Results

Image segmentation using the Hough transform was performed by manually entering a separate radius search range for each of the fifty images. This was done because if a common radius search range was given for all the images, the transform tended to segment circles of larger radii among images with smaller pupil sizes. As a result, false pupil boundaries were being detected which was undesirable.

While carrying out manual input of radius search range to the Hough transform, the pupil boundary was detected without much difficulty. A few images had pupil distortion due to large amounts of pigment being lost from the iris [5], causing the pupil to not be perfectly circular. In these cases, a segmentation that left out as much of the distorted region as possible was selected. The outer iris boundary in some images was not clearly visible and appeared diffused into the sclera region. It was then decided that including extra pixels in the segmentation would be better than discarding useful pixels, that is, the iris transillumination defect regions.

A list of the parameter values for each subject's eye image showing the inputs to the Hough transform in order to segment out the iris regions is given in appendix Table A.2. The pupil boundaries and centers were detected first using the minimum and maximum radius search range, and using these center coordinates, the outer iris boundaries were detected. In all cases, the search was limited to one circle. Each image took approximately ten minutes to segment correctly.

At the end of the segmentation stage, fifty iris images were created with all pixels not belonging to the iris region replaced by black pixels as seen in Figure 4.1 (b). Mild

distortion of the pupil can be seen in Figure 4.1 (a). The segmented iris images were then converted to polar coordinates and an example is shown in Figure 4.1 (c).

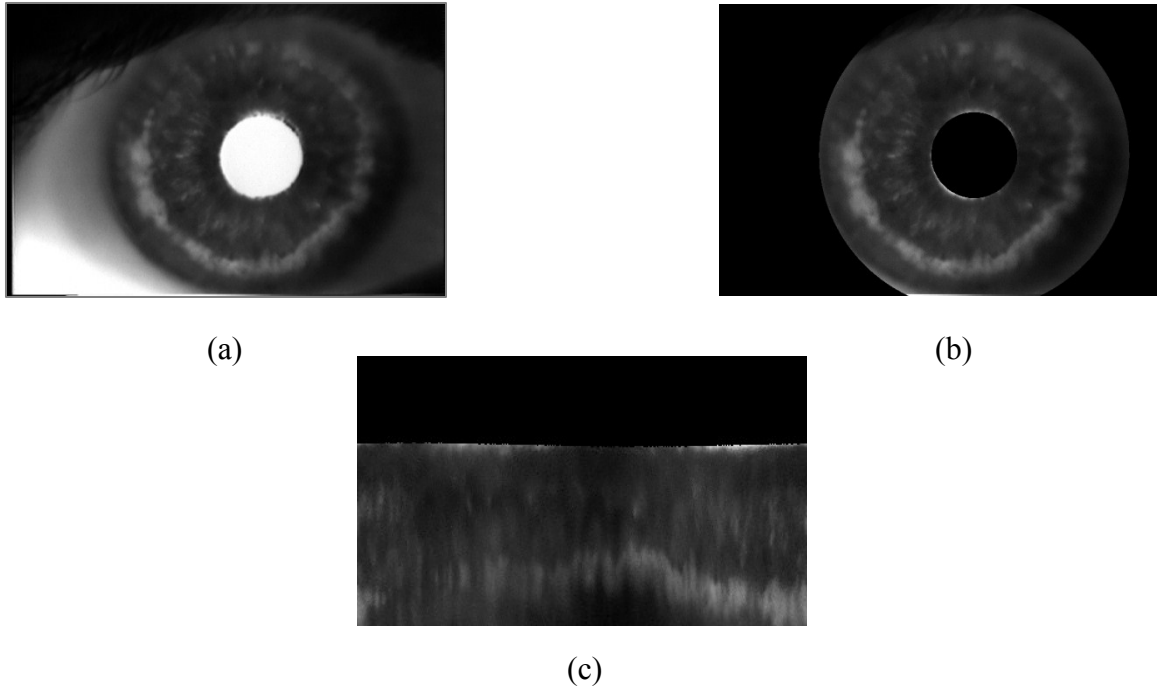


Figure 4.1: Image segmentation result example: (a) The original eye image for subject number 14. (b) The iris extracted by the Hough transform with pupil radius 72 pixels and outer iris radius 255 pixels. (c) The extracted iris region converted to polar coordinates.

4.2 Feature Calculation Results

The feature calculation stage was implemented using the Insight Toolkit (ITK). Before calculation of features, the polar image boundaries against a black background had to be mirrored to prevent the kNN classifier from falsely classifying image

boundaries as defect regions. After mirroring 10 rows of the image above and below the boundaries, feature calculation was carried out. Following calculation of features, random selection of training pixels was performed as described in Section 3.4. These pixel values were then written into a text file to be given as input for the training stage of the classifier. For the testing data, pixels from the test feature images were selected and stored in text files. The feature calculation results took ten minutes to obtain per feature image.

The calculated features are shown in Figure 4.2:

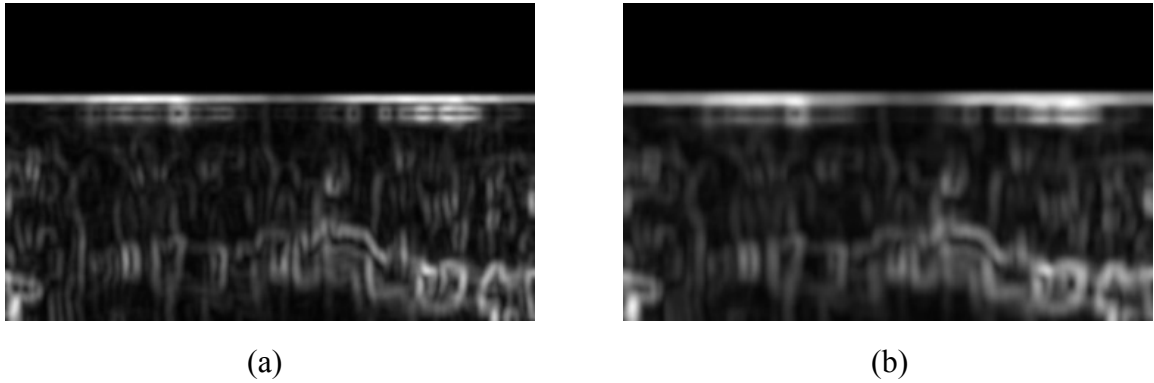
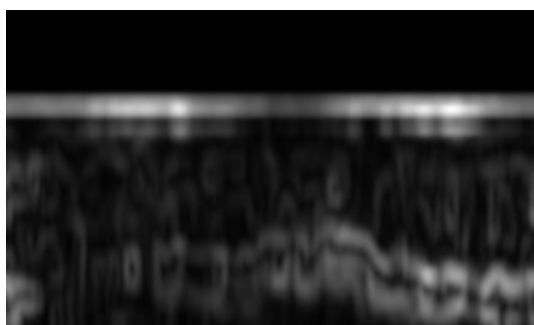
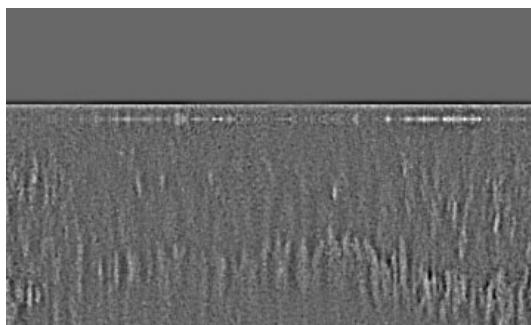


Figure 4.2: Feature calculation results examples: (a) Standard deviation with a neighborhood of 3x3. (b) Standard deviation with a neighborhood of 5x5. (c) Standard deviation with a neighborhood of 3x9. (d) Difference of Gaussians with $\sigma_1 = 1$ and $\sigma_2 = 2$. (e) Difference of Gaussians with $\sigma_1 = 2$ and $\sigma_2 = 4$. (f) Gradient Magnitude image. (g) Average intensity image. (h) Gaussian derivative of image along the X-axis. (i) Gaussian derivative of image along the Y-axis. (j) Laplacian of image.

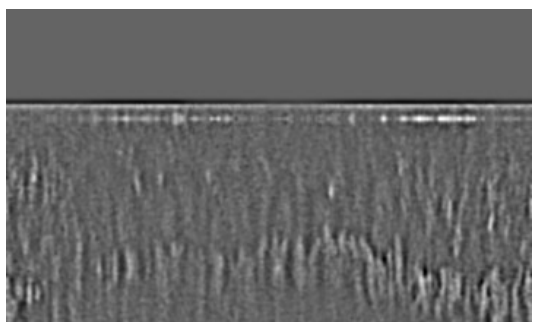
Figure 4.2 continued -



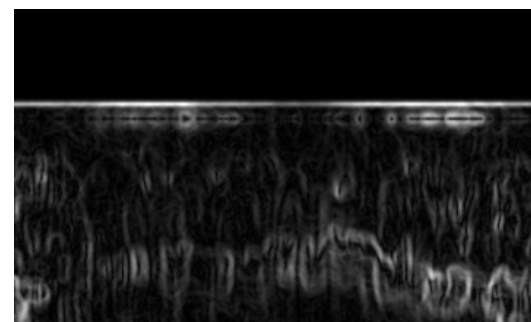
(c)



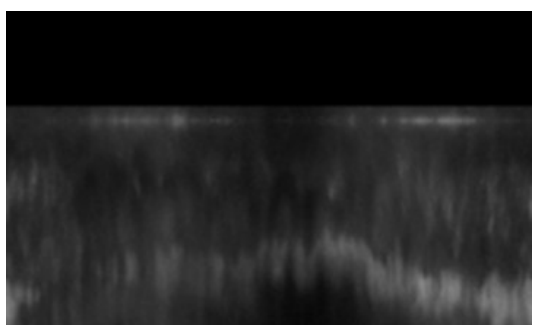
(d)



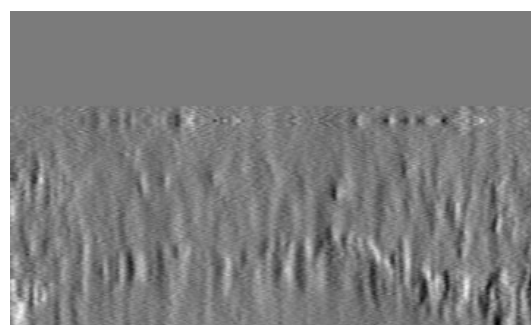
(e)



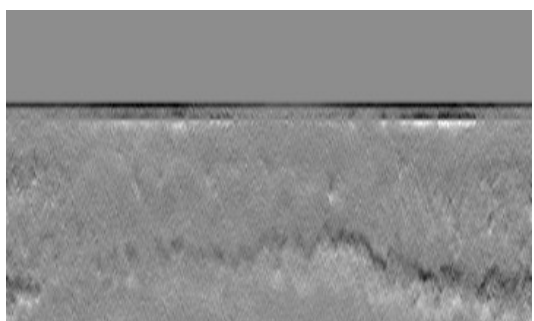
(f)



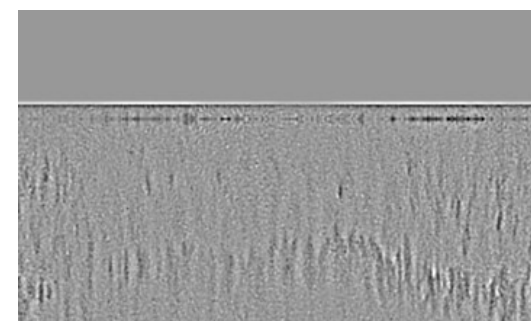
(g)



(h)



(i)



(j)

4.3 Feature Selection Results

After the feature calculation process, feature selection was carried out using WEKA. The algorithm used was linear forward selection with cross validation. The output of feature selection showed that the difference of Gaussians applied to an image with $\sigma_1 = 1$ and $\sigma_2 = 2$, the Gaussian Derivative of an image in the vertical direction and the Laplacian of an image were not optimal features. Seven features remained to perform kNN classification. Feature selection in WEKA was a quick process of a few minutes.

4.4 KNN Classification Results

Following the testing of the kNN classifier, using $k = 21$, a probability image was obtained for each of thirty test images, with 21 gray levels ranging from 0 to 255.

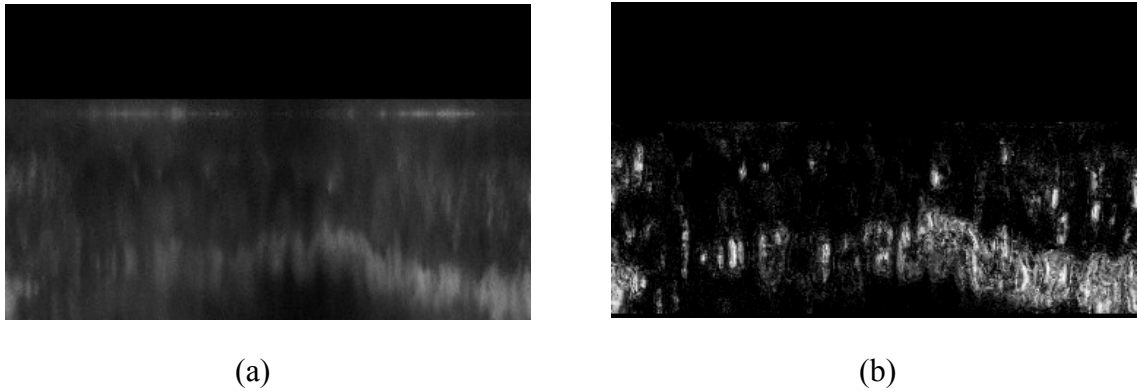


Figure 4.3: KNN classification results example: (a) The segmented iris region in the polar domain for participant number 14. (b) The probability image with 21 gray levels showing the likelihood of each pixel belonging to a defect region. (c) The probability image converted back to the Cartesian domain. (d) The reference standard image with defect regions manually outlined.

Figure 4.3 continued –



A pixel with a higher gray level has a higher probability of belonging to a defect region. The images were then converted back to the Cartesian domain. As seen in Figure 4.3 (b) and (c), the iris transillumination defect regions have been identified by the kNN classifier with some false positives present as well.

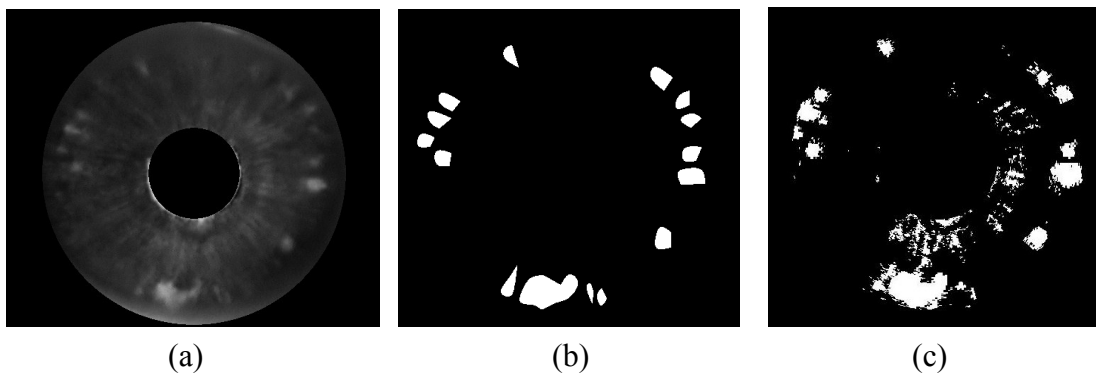
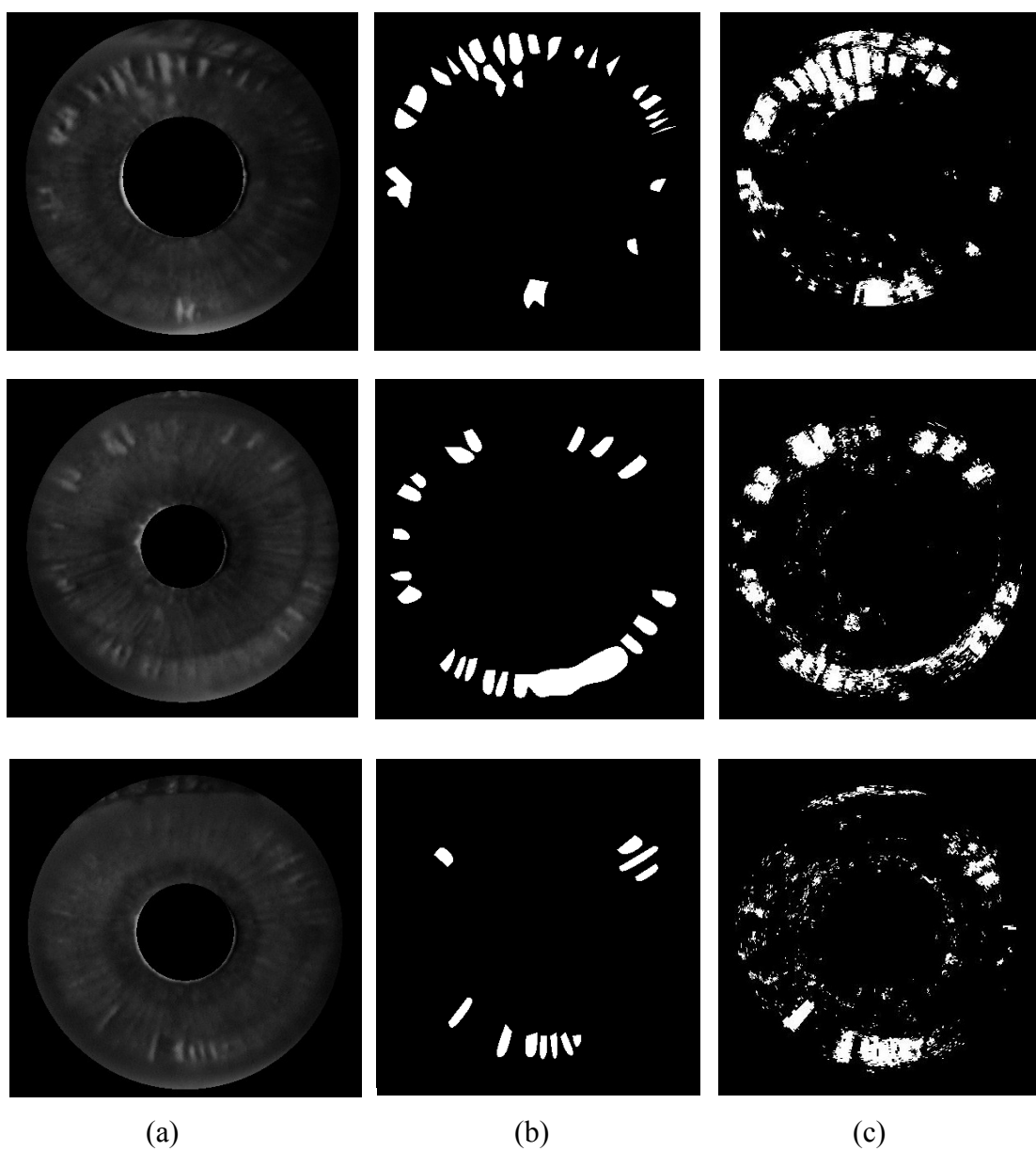


Figure 4.4: Some results of the kNN classification: (a) This column of images is the iris regions that were manually segmented out for subject numbers 9, 16, 40 and 43. (b) The reference standard images showing the defect regions manually outlined. (c) The probability images with a threshold of 3/21 applied.

Figure 4.4 continued -



Some more classification results have been shown along with their corresponding reference standard images in Figure 4.4 above.

The area under the curve (AUC) is a measure of the performance of a diagnostic test that plots sensitivity (true positive rate) versus 1-specificity (false positive rate). An AUC of 0.5 indicates a test that is equivalent to tossing a coin while an AUC of 1 indicates a test that has 100% sensitivity with no false negatives and 100% specificity with no false positives.

An AUC of 0.901 was obtained for the fitted ROC curve for a data set of thirty images using $k = 21$ as shown in Figure 4.5.

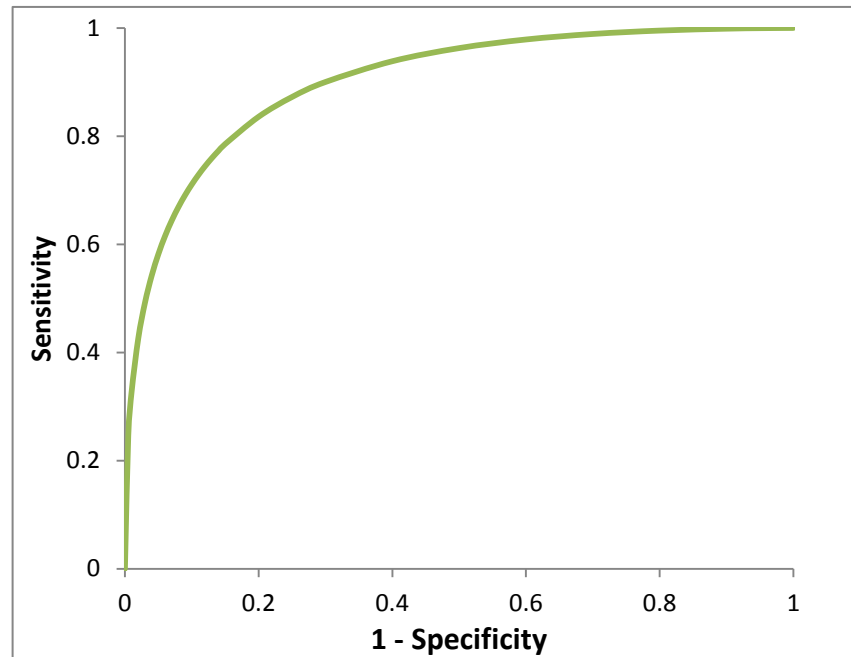


Figure 4.5: The ROC curve for the kNN classification output.

The kNN classification process was executed using a higher value of $k = 101$ and the ROC curve was plotted using the results. This was done to determine whether higher

values of k would produce a higher value of the AUC. The result of the AUC of the fitted ROC curve was equal to 0.907 which was similar to the result of using $k = 21$. Thus, the results showed no sensitivity to the use of a higher value of k .

The ROC curve can be used to select the best operating point. This point can be chosen such as to give the best tradeoff between the costs of failing to detect positives against the cost of raising false alarms.

CHAPTER 5

DISCUSSION

The method described in this thesis for using pixel classification to quantify the amount of transillumination in an eye has not been attempted before and it improves upon the bias of a human observer manually marking defects, as well as resulting in saved time. This test serves as a measure of automatically finding regions of pigment dispersion without having to take into consideration inter-observer variability.

The large AUC value of 0.901 using $k = 21$ indicates that pixel classification of iris transillumination defects is an accurate technique which has the potential to be used for CAD of the Pigment Dispersion Syndrome.

Reducing the number of false positives in the output would result in a higher value of the AUC. This could be done by adding features to the classifier training set that are not solely dependent on intensity changes.

CHAPTER 6

CONCLUSION

Iris transillumination defects caused by pigment dispersion syndrome can be successfully detected by using pixel classification with the kNN algorithm. Future work could include adding more useful features to improve the AUC by reducing the number of false positives. Different classifiers could be used to determine if the classification of defects can be improved. The manual segmentation of the iris regions could be fully automated by modifying the Hough transform algorithm so that it does not show a bias for detecting circles with a larger radius. Testing the method described in this thesis on a larger dataset could show whether the algorithm can consistently maintain its accuracy. The percent transillumination of the iris can be calculated, and a correlation between this value and the age of the subject can be investigated. Also, the changes in transillumination defects' sizes and the pupil size can be tracked over time.

APPENDIX

Table A.1: The data of 38 out of 50 subjects included in this research with their diagnoses as follows - *PG*: Pigment Dispersion Syndrome with elevated pressures and glaucomatous nerves, *PDS*: Pigment Dispersion Syndrome with normal pressure and nerves, *PDS w/ OHT*: Pigment Dispersion Syndrome with elevated pressures but normal nerves.

Participant Number	Year of Birth	Year of Diagnosis	Age when Diagnosed	Diagnosis
1	1973	1991	18	PDS
2	1955	1999	44	PDS w/ OHT
3	1962	1993	31	PG
4	-	-	-	-
5	-	-	-	-
6	-	-	-	-
7	-	-	-	-
8	1928	1990	62	PG
9	-	-	-	-
10	1946	1990	44	PG
11	1962	1993	31	PG
12	1924	1988	64	PG
13	1937	1974	37	PG
14	1929	1979	50	PG
15	1958	1996	38	PDS
16	1956	1992	36	PDS
17	1931	1996	65	PG
18	1955	1999	44	PDS w/OHT
19	1949	1999	50	PDS w/OHT
20	1946	1980	34	PDS
21	1953	1992	39	PDS
22	-	-	-	-
23	1973	1991	18	PDS
24	1962	1993	31	PG
25	1928	1980	52	PG
26	1951	1993	42	PDS

¹Table A.1 continued:

Participant Number	Year of Birth	Year of Diagnosis	Age when Diagnosed	Diagnosis
27	1941	1995	54	PDS
28	1923	1992	69	PDS
29	1938	1986	48	PG
30	1952	1992	40	PG
31	1924	1987	63	PG
32	1959	1988	29	PG
33	1951	1989	38	PDS w/OHT
34	1957	1985	28	PDS
35	-	-	-	-
36	1927	1992	65	PG
37	1951	1994	43	PDS
38	1967	1995	28	PDS
39	1961	1991	30	PG
40	1952	1992	40	PDS
41	1953	1995	42	PG
42	-	-	-	-
43	1962	1992	40	PDS
44	-	-	-	-
45				
46	1967	1995	28	PG
47	-	-	-	-
48	1946	1998	52	PG
49	1962	1998	36	PDS
50	1964	1988	24	PG

¹The data of each subject included in this research with their diagnoses.

Table A.2: A list of the parameter values for each subject's eye image showing the inputs to the Hough transform in order to segment out the iris regions, with each value representing the number of pixels.

Participant Number	Pupil			Iris			
	Min Radius	Max Radius	Radius Detected	Min Radius	Max Radius	Center (x, y)	Radius Detected
1	30	120	92	150	290	(366, 258)	227
2	10	50	31	120	200	(503, 210)	170
3	25	90	57	100	220	(448, 225)	172
4	15	75	41	140	290	(330, 225)	206
5	35	100	63	140	290	(370, 233)	199
6	40	100	70	140	290	(359, 205)	198
7	35	100	61	150	290	(411, 203)	217
8	30	80	53	100	210	(321, 308)	169
9	35	100	66	150	290	(346, 262)	215
10	25	105	73	140	290	(393, 238)	188
11	56	120	84	100	230	(374, 224)	163
12	50	110	80	150	290	(356, 226)	221
13	25	105	75	180	320	(337, 250)	244
14	25	105	70	150	350	(419, 248)	256
15	30	90	58	150	290	(326, 282)	219
16	25	105	74	140	290	(439, 204)	197
17	35	100	65	150	280	(408, 238)	220
18	30	80	58	100	240	(365, 191)	176
19	35	100	64	100	230	(408, 289)	166
20	65	125	95	140	260	(320, 294)	205
21	50	110	77	140	290	(413, 279)	194
22	30	90	57	150	340	(317, 239)	239
23	25	105	74	100	180	(503, 191)	148
24	30	80	56	100	200	(258, 222)	155
25	40	100	71	120	270	(407, 212)	195
26	15	75	45	100	200	(287, 242)	164
27	56	116	86	180	300	(420, 245)	245
28	30	75	50	100	240	(310, 154)	168

²Table A.2 continued:

Participant Number	Pupil			Iris			
	Min Radius	Max Radius	Radius Detected	Min Radius	Max Radius	Center (x, y)	Radius Detected
29	30	80	52	100	180	(351, 167)	141
30	30	80	55	140	290	(304, 278)	207
31	40	100	65	150	280	(404, 245)	214
32	10	75	47	150	280	(368, 283)	225
33	20	80	50	100	180	(412, 269)	149
34	50	110	83	100	230	(334, 293)	168
35	50	110	77	140	290	(370, 183)	193
36	15	75	47	140	290	(336, 206)	185
37	50	110	81	150	290	(386, 233)	217
38	40	100	71	150	340	(395, 233)	244
39	50	110	78	150	320	(400, 242)	228
40	30	75	51	140	290	(402, 258)	189
41	40	100	69	150	290	(337, 214)	228
42	30	75	50	140	290	(332, 221)	185
43	35	100	60	140	290	(411, 275)	194
44	30	90	57	140	290	(350, 194)	205
45	40	100	68	150	280	(407, 240)	211
46	20	80	49	80	180	(414, 228)	138
47	50	110	83	140	290	(297, 247)	199
48	75	140	104	180	370	(337, 229)	256
49	5	70	37	80	150	(431, 275)	118
50	65	125	93	140	290	(348, 265)	183

²A list of the parameter values for each subject's eye image showing the inputs to the Hough transform in order to segment out the iris regions, with each value representing the number of pixels.

REFERENCES

- [1] National Eye Institute. "Glaucoma: What you should know." Internet: <http://permanent.access.gpo.gov/lps110153/webGLAUC.pdf>, 2012 [3/12/2003].
- [2] Wallace L.M. Alward, *Glaucoma: The Requisites in Ophthalmology*. Mosby, Inc., 2000, pp. 132-136.
- [3] W.L Haynes, W.L.M. Alward, J.K. McKinney, P.M. Munden, R. Verdict. "Quantitation of iris transillumination defects in eyes of patients with pigmentary glaucoma." *Journal of Glaucoma*, vol. 3, pp. 106-113, 1994.
- [4] W.L.M Alward, P.M. Munden, R.E. Verdict, R. Perell, H.S Thompson. "Use of infrared videography to detect and record iris transillumination defects." *Archives of Ophthalmology*, vol. 108, May 1990.
- [5] W.L. Haynes, W.L.M. Alward, H.S Thompson, "Distortion of the Pupil in Patients with the Pigment Dispersion Syndrome." *Journal of Glaucoma*, vol. 3, pp. 329-332, 1994.
- [6] J.C. Morrison and I.P. Pollack, "The Glaucomas," in *Glaucoma Science and Practice*, New York: Thieme Medical Publishers, 2003, pp. 207-208.
- [7] E.P. Widmaier, H. Raff and K.T. Strang, *Vander's Human Physiology*. McGraw-Hill, 2006, pp. 229-238.
- [8] H.G. Scheie and J.D. Cameron, "Pigment Dispersion Syndrome: A Clinical Study." *British Journal of Ophthalmology*, vol. 65, pp. 264-269, 1981.
- [9] D.A. Lee and E.J. Higginbotham, "Glaucoma and its treatment: A review." *American Journal of Health-System Pharmacy*, vol. 62(7), pp. 691-699, 2005.
- [10] D.K. Roberts, A. Lukic, Y. Yang, J.T. Wilensky, M.N. Werwick, "Multispectral Diagnostic Imaging of the Iris in Pigment Dispersion Syndrome." *Journal of Glaucoma*, pp. 1, 2011.
- [11] C.U. Richter, T.M. Richardson and W.M. Grant, "Pigmentary Dispersion Syndrome and Pigmentary Glaucoma." *Archives of Ophthalmology*, vol. 104, 1986.
- [12] K. Mosaliganti, A. Gelas, P. Cowgill and S. Megason. (2009, September). "An Optimized N-Dimensional Hough Filter for Detecting Spherical Image Objects." *The Insight Journal*. [Online]. 2009 July-December. Available: <http://hdl.handle.net/10380/3129> [April 9, 2012].
- [13] M.A. Christopher, "Truthmarker: A tablet-based approach for rapid image annotation." M. S. Thesis, The University of Iowa, Iowa City, 2011.

- [14] D. M. Mount and S. Arya, "ANN Programming library", ANN, Version 1.1.2, Released 27 Jan 2010, <http://www.cs.umd.edu/~mount/ANN/>
- [15] Eye anatomy, <http://drjgriffin.com/no-stitch-cataract/>
- [16] J. Sowka, "Pigment dispersion syndrome and pigmentary glaucoma." *Optometry - Journal of the American Optometric Association*, vol. 75(2), pp. 115-122, 2004.
- [17] M. Dash and H.Liu, "Feature Selection for Classification." *Intelligent Data Analysis I*, pp. 131-156, 1997.
- [18] M. Gutlein, E. Frank, M. Hall, A. Karwath, "Large-scale attribute selection using wrappers." *IEEE Symposium on Computational Intelligence and Data Mining*, 2009, pp. 332-339, 2009.
- [19] X. Xu, M.K. Garvin, M. D. Abràmoff and J.M. Reinhardt, "Simultaneous Automatic Detection of the Optic Disc and Fovea on Fundus Photographs." *Proceedings of SPIE*, vol. 7962, 2011.
- [20] M.D. Abràmoff, J.M. Reinhardt, S.R. Russell, J.C. Folk, V.B. Mahajan, M. Niemeijer and G. Quellec, "Automated Early Detection of Diabetic Retinopathy." *Ophthalmology*, vol. 117(6), pp. 1147-1154, 2010.
- [21] M.D. Abràmoff, W.L. M. Alward, E.C. Greenlee, L. Shuba, C.Y. Kim, J.H. Fingert and Y. H. Kwon, "Automated Segmentation of the Optic Disc from Stereo Color Photographs Using Physiologically Plausible Features." *Investigative Ophthalmology and Visual Science*, vol. 48(4), pp. 1665-73, 2007.
- [22] R. Bock, J. Meier, L.G. Nyúl, J. Hornegger and G. Michelson, "Glaucoma risk index: Automated glaucoma detection from color fundus images." *Medical Image Analysis*, vol. 14(3), pp. 471-481, 2010.
- [23] J. Eng, ROC analysis: Web-based calculator for ROC curves. Retrieved 5/2/12, from <http://www.jrocfits.org>.
- [24] M. Hall, E. Frank, G. Holmes, B. Pfahringer, P. Reutemann, I.H. Witten, "The WEKA Data Mining Software: An Update." *SIGKDD Explorations*, vol. 11(1), 2009.
- [25] S. Bodduluri, "Analysis of Chronic Obstructive Pulmonary Disease (COPD) Using CT Images." M. S. Thesis, The University of Iowa, Iowa City, 2012.
- [26] I. Reiser, R.M. Nishikawa, M.L. Giger, J.M. Boone, K.K. Lindfors and K. Yang, "Automated detection of mass lesions in dedicated breast CT: A preliminary study." *Medical Physics*, vol. 39 (2), 2012.
- [27] H. Zhang, "Segmentation And Computer-aided Diagnosis of Cardiac MR Images Using 4-D Active Appearance Models". PhD Thesis, The University of Iowa, Iowa City, 2007.

- [28] J. Staal, M.D. Abramoff, M. Niemeijer, M.A. Viergever and B. van Ginneken, "Ridge-based vessel segmentation in color images of the retina." *IEEE Transactions in Medical Imaging*, vol. 23(4), pp. 501-509, 2004.
- [29] J.H. Fingert, J.H. Burden, K. Wang, Y.H. Kwon, W.L.M. Alward and M.G. Anderson, "Circumferential Iris Transillumination Defects in Exfoliation Syndrome." *Journal of Glaucoma*, pp. 1, 2012.
- [30] D.K. Roberts and M.N. Wernick, "Infrared imaging technique may help demonstrate iris transillumination defects in blacks who show other pigment dispersion syndrome clinical signs." *Journal of Glaucoma*, vol. 16(5), pp. 440-447, 2007.
- [31] D.K. Roberts, "Digital infrared photography assists in the detection of iris and ciliary body cysts." *Journal of Glaucoma*, vol. 12(3), pp. 288-291, 2003.
- [32] J. Canny, "A Computational Approach to Edge Detection." *IEEE Transactions on Pattern Analysis and Machine Intelligence*, vol. PAMI-8(6), pp. 679-698, 1986.
- [33] A. Beghdadie and A. Le Negrat, "Contrast enhancement technique based on local detection of edges." *Computer Vision, Graphics and Image Processing*, vol. 46(2), pp. 162-174, 1989.
- [34] D. Marr and E. Hildreth, "Theory of edge detection." *Proceedings of the Royal Society of London. Series B, Biological Sciences*, vol. 207(1167), pp. 187-217, 1980.